Chemical Science

Accepted Manuscript

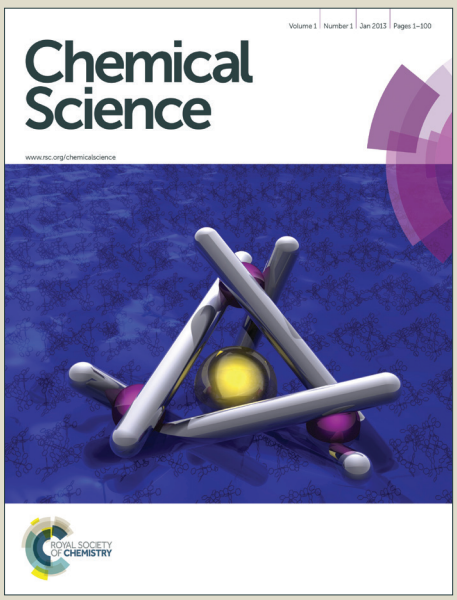

ROYAL SOCIETY OF CHEMISTRY

www.rsc.org/chemicalscience

Angle-resolved valence shell photoelectron spectroscopy of neutral nanosized molecular aggregates

Ruth Signorell, Bruce L. Yoder, Adam H. C. West, Jorge J. Ferreiro, Clara-Magdalena Saak*

ETH Zürich, Laboratory of Physical Chemistry, Wolfgang-Pauli-Strasse 10, CH-8093, Zürich, Switzerland

Chemical Science

Date: 22 January, 2014

Keywords: asymmetry parameter, beta parameter, anisotropy parameter, cluster, Na-doping method, vacuum ultraviolet light, velocity map imaging

Table of contents entry: Angle-resolved photoelectron spectroscopy opens a new avenue to probe the orbital character of solutes and solvents from the nanoscale to the bulk.

* To whom correspondence should be addressed. E-mail: rsignorell@ethz.ch

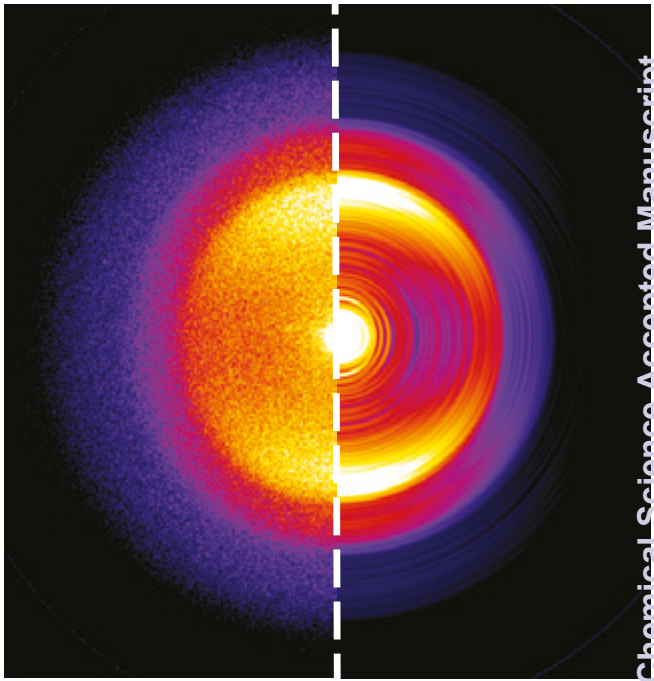

ABSTRACT

This mini-review provides an overview of the recent developments in the field of angle-resolved photoelectron spectroscopy of neutral weakly-bound molecular aggregates with sizes that range from the gas phase monomer into the lower nanometre regime. A summary of the recent first size-dependent studies of neutral single-component and solute/solvent nano-clusters in the valence-shell region is provided. The challenges in determining independent information on the particle size as well as accurate angular-dependent information are highlighted. Examples of potential artefacts that falsify the true photoelectron angular distribution are discussed.

1. Introduction

As a standard method photoelectron (PE) spectroscopy can provide information on the electronic structure of a broad variety of different physical/chemical systems with relevance in diverse fields ranging from astrophysics to industrial applications. Band positions (binding energies (BEs); ionisation energies (IEs)) and bandwidths in photoelectron spectra contain information on the chemical composition and structural features of such systems. Much less common is the determination of the photoelectron angular distribution (PAD), even though it provides important complementary information on orbital character/hybridisation. The fact that less attention has been paid to the PAD is a consequence of the challenges in determining experimental angular information and in the modelling and analysis of the data.

The sensitivity to the orbital character/hybridisation makes angle-resolved PE spectroscopy an attractive tool for the investigation of size-dependent properties that evolve when a system changes its size from the molecular to the macroscopic bulk regime. For example, confinement effects on solute distribution and on intermolecular structures in nano-solutions of different size are of central interest for a clearer understanding of chemical reactions at interfaces and in the condensed phase in general. Size-dependent PE studies of molecular aggregates, however, pose several challenges. The targeted formation of molecular aggregates with sizes that vary systematically from small oligomers to the nanometre or even sub-micrometre regime can be a demanding task. Size-selection or at least size-determination is the essential next step for size-dependent studies. The fact that size-selection for *charged* aggregates is possible provides one explanation why more size-dependent PE studies have so far been performed on anionic aggregates (refs. [1-5] and references therein) than on neutral aggregates (refs. [6-15] and references therein). Another reason is the availability of appropriate light sources in the laboratory. Compared with typical ionisation energies of neutral

aggregates, those of anionic clusters are readily accessible with laser light sources in the laboratory. Ionisation of the valence shell of neutral molecular systems, by contrast, usually requires vacuum ultraviolet (VUV) light while inner shell ionisation needs even higher energies. Since corresponding laser light sources are not commercially available, PE studies of neutral aggregates often rely on the availability of synchrotron radiation sources. The difficulties associated with the measurement of reliable angular-dependent data and in particular with the analysis of these data is common to both neutral as well as anionic aggregates[1-4, 8, 10, 11, 14-18] (and references therein). It is still a challenge to record PADs without distorting the trajectories of the photoelectrons in an uncontrolled way and thus falsifying the measurement. The difficulties with the data analysis arise from the fact that the PAD depends on the type of the orbital from which the photoelectron originates and (through transition matrix elements and partial wave interference) on the photoelectron kinetic energy (eKE). In aggregates, elastic and inelastic intracluster scattering processes presumably have a crucial influence on the PAD.[8, 10, 11, 14-16, 19-21] All factors depend on the degree of condensation/solvation and hence on the aggregate size.

The current mini-review focuses on angle-resolved valence-shell PE studies of neutral weakly-bound molecular aggregates with sizes that range from the gas phase monomer into the lower nanometre regime (< 10 nm diameter). To the best of our knowledge, only three investigations that provide angular information for neutral aggregates have been published so far.[11, 14, 15] In addition, we present new results on angle-resolved PE spectra of nano-solutions, the details of which will be the subject of forthcoming publications. More work than for neutral molecular aggregates is available for large neutral rare gas clusters (see ref.[21] and references therein). Comparison with results from rare gas studies are made where they are useful. Note that we do not review inner-shell PE studies and PE investigations of small neutral clusters. The different experimental setups used for angle-resolved PE studies of

neutral aggregates are briefly summarised in section 2.1. Section 2.2 addresses the issues associated with the independent determination of the aggregate size. In this context, the "Na-doping" method is discussed in some detail.[14, 22-26] It was originally proposed by Buck and coworkers[22-24] and seems currently the best solution to obtain independent size information. General trends in the evolution of IEs and bandwidths with changing aggregate size are summarised in Section 3. Finally, Section 4 is devoted to angle-dependent information and to the issue of artefacts in PAD measurements.

2. Experimental setups

2.1 Photoelectron spectrometers and light sources

Only few experimental setups for angle-resolved photoelectron spectroscopy of large weakly-bound neutral molecular and rare gas clusters have been reported so far[8, 10, 11, 14-16] (and references therein). The purpose of this subsection is to summarise similarities and differences of the different setups. As an example, Fig. 1 shows a sketch of the setup in our laboratory. In general, aggregates are produced by supersonic expansion of neat substance vapour or a substance vapour/rare gas mixture through a nozzle. Various types of nozzles with different shapes, sizes, and lengths are used either in continuous or pulsed mode to generate aggregates of different sizes. The source chamber with the nozzle is usually separated by a skimmer from the other vacuum chambers, through which the cluster beam passes downstream (see Fig. 1). To date, two different schemes have been employed for ionisation and photoelectron detection:

(i) The clusters are ionised by synchrotron radiation and the kinetic energies of the emitted photoelectrons are determined with the help of hemispherical electron analysers[11, 16] or time-of-flight electron spectrometers.[8, 10] To record the photoelectron angular distribution (PAD) either the spectrometer[16] or the polarisation axis of the synchrotron radiation[11] is rotated, or multiple spectrometers are used.[8, 10] As described in section 4, the asymmetry parameter, commonly called β-parameter, is usually reported to quantify the PAD. Similar setups as the ones described above are used for angle-resolved photoelectron spectroscopy with liquid microjets.[27-30] Either a high harmonic laser light source or synchrotron radiation is used in these studies.

(ii) Vacuum ultraviolet (VUV) laser light (also referred to as EUV or XUV light) or UV laser light is used to ionise the clusters and the electron kinetic energy (eKE) and PAD are determined by velocity map imaging (VMI).[31] A scheme of our experimental setup is shown in Fig. 1 (see ref.[14, 15] for details). We use nanosecond lasers (20 Hz) for cluster ionisation in the ionisation chamber with energies ranging from the VIS/UV to ~ 18 eV. The VIS/UV light ($\geq$ 202 nm) is generated by doubling or tripling the output of a dye laser. Alternatively, for some experiments the fourth harmonic (266 nm) of a portable Nd:YAG laser is used. The VUV light is generated by resonance enhanced two-color 4-wave-mixing (sum frequency and difference frequency mixing) in a pulsed rare gas (Xe, Kr, Ar) beam using the corresponding $^2P_{3/2}$ and $^2P_{1/2}$ two-photon resonances. The (fundamental, doubled or tripled) outputs of two dye lasers (ν_1 and ν_2) pumped by 355 or 532 nm light from a single, pulsed Nd:YAG laser are mixed in the rare gas jet (4-wave-mixing chamber in Fig. 1). The desired sum frequency ($2\nu_1+\nu_2$, $3\nu_1$) or difference frequency ($2\nu_1-\nu_2$) light is separated from other frequencies generated in the non-linear process and from the fundamentals (ν_1 and ν_2) by a stepper-motor driven, toroidal diffraction grating in the grating chamber and coupled into the ionisation chamber through a pinhole. The VUV light source is tunable (by tuning ν_2) with a bandwidth

of ≤ 0.7 cm^{-1}; however, the light intensity can vary strongly as a function of the photon energy.[32] The propagation direction of the light and the direction of polarisation lie in a plane parallel to the imaging detector plane. Cylindrical symmetry parallel to the detector plane (given by the polarisation axis of the light) is essential for two-dimensional VMI measurements because it allows the retrieval of the three-dimensional velocity distribution of photoelectrons from the measured two-dimensional projection (raw image) on the imaging detector.[31, 33-35] For electron imaging, the repeller and extractor voltages (HV extractor in Fig. 1) are optimised for VMI conditions so that photoelectrons with the same initial velocity component parallel to the detector plane are mapped onto the same spot on the detector irrespective of their "birth" position. The two-dimensional position sensitive imaging detector consists of a pair of 40 or 75 mm diameter multichannel plates (MCPs) which are coupled to a phosphor screen. The luminescence of the phosphor screen is captured by a charge-coupled device (CCD) camera. For the results presented in this review, BASEX[34] and pBASEX[35] are used for the reconstruction of raw images to determine the eKE and the PAD (β-parameter see section 4). Kinetic energy calibration of the images is performed using photoelectron spectra of Xe gas as a reference.[14] Similar VMI setups are used for photoelectron spectroscopy of anionic clusters.[1-5]

Advantages of scheme (i) over scheme (ii) are the higher and uniform photon flux, as well as a broader range of photon energy of synchrotron radiation compared with laser light sources. These advantages reduce the measurement time and allow for the investigation not only of valence but also of inner shell electrons. The advantages of combining VMI with laser light sources (scheme (ii)) are the simplicity of the setup, the availability in the laboratory, and the high resolution that can be achieved in principle.

2.2 Determination of aggregate size

To obtain meaningful results from size-dependent photoemission studies of clusters and nanosized particles, it is crucial to know the size of the aggregates. This is particularly challenging for large, neutral, weakly-bound aggregates. Size-selective photoemission studies of large, neutral aggregates are not feasible nowadays because size-selection before the actual photoemission experiment as performed for charged aggregates[1-5] is not possible. Even determination of the size-distribution of neutral weakly-bound aggregates already poses a major challenge. Many particle sizing techniques are not 'soft' enough for weakly-bound systems and thus do not allow one to record the original size distribution destruction free (see discussion in refs.[25, 26]). Usually, scaling laws are used to estimate the average aggregate size in photoemission experiments of neutral systems.[6, 11, 12] Scaling laws are empirical laws determined from mass spectrometric measurements that describe the dependence of the mean cluster size from the nozzle conditions (nozzle type, pressure, temperature).[10, 16, 19-21, 23, 36-39] They provide approximate information on the average particle size but no detailed size-distribution. The accuracy of the average size is assumed to be less good for molecular aggregates than for rare gas clusters. Unfortunately, publications rarely specify the accuracy of scaling laws when applied to molecular systems although possible errors seem to be substantial.[9, 11, 13, 38]

We have recently proposed to determine the size distribution of molecular aggregates *in situ* using the "Na-doping method" before and after each photoemission experiment in an attempt to overcome the issues arising from insufficient size information.[14, 15] *In situ* means that the sizes of the aggregates are determined at the same spatial and temporal position in the cluster beam where photoemission takes place, i.e. the same experimental delay time and position between the repeller and the extractor plates (see Figs. 1 and 2). This is crucial for supersonic expansions for which the aggregate size varies sensitively with the distance from

the nozzle (evaporation) and the exact timing (for pulsed expansions). Fig. 2 shows a sketch of the working principle of the Na-doping method. During aggregate size measurements via the Na-doping method, the Na-oven in the Na-oven chamber (Fig. 1) is held at a temperature of ~ 480 K to maintain a local Na vapour pressure of ~10^{-4} mbar. Under these conditions, a certain fraction of the clusters/particles that traverse the Na-oven pick up a single Na atom. The Na in these Na-cluster/particle complex is then ionised with a relatively low-energy UV photon (< 5 eV, typically 4.66 eV), the energy of which is too low to ionise the undoped cluster/particle itself. The mass of the Na-cluster/particle complexes in the beam is then determined by mass spectrometry resulting in a cluster/particle mass distribution after subtraction of 23 mass units for the Na. This cluster/particle mass distribution can be converted to a cluster/particle size distribution if the density and the shape of the aggregate are known or corresponding assumptions are made. As mentioned, particle sizing is performed just before and after each photoemission experiment. For photoemission experiments of undoped aggregates (section 3.1) the heating in the Na oven is turned off to avoid Na pick-up.

The Na-doping method was originally proposed by Buck and coworkers.[22-24] They demonstrated for nanosized rare gas and ammonia aggregates that the Na-doping method is much softer than electron impact ionisation at electron energies between 50 and 1500 eV, which causes substantial fragmentation of the original clusters. One might argue here that it is not surprising that the Na-doping method is softer than electron impact using such high electron energies and that this comparison does not prove that the Na-doping method is a soft ionization method for neutral weakly-bound molecular aggregates. By comparing the Na-doping method with single photon ionisation just above the lowest ionisation threshold of the undoped aggregates using VUV laser light, we have shown that the Na-doping method is indeed soft and cannot be replaced by threshold ionisation methods.[25, 26] A major reason why

threshold ionisation in combination with mass spectrometry is in general not suitable for cluster/particle sizing are post-ionisation, intracluster reactions that can lead to substantial cluster decay and thus falsify the measured size distributions (see discussion in ref.[26]). The example in Fig. 3 compares the size distribution measured with the Na-doping method (top) with the size distribution recorded after VUV threshold ionisation (bottom) for the same acetic acid (HAc) cluster beam. The Na-doping leaves the original cluster size distribution largely intact while VUV ionisation causes substantial cluster decay so that no useful size information is left. The substantial cluster decay in the latter case can be explained by the intracluster chain reaction (2) that occurs after an initial fast intermolecular proton transfer in the ionic state (1). The acetyloxy radical formed in (1) can catalyse the decay of HAc into carbon dioxide and methane (2), which can easily evaporate from the cluster. The chain reaction (2) can happen many times in a cluster and since each cycle releases 36 kJ/mol (0.37 eV) it has the capacity to self-propagate and/or to evaporate HAc molecules from the cluster.[26]

$CH_3CO_2H^+ + CH_3CO_2H \rightarrow CH_3CO_2 + CH_3CO_2H_2^+$ $\Delta_r H \sim -0.78$ eV (1)

$CH_3CO_2H = CO_2 + CH_4$ $\Delta_r H \sim -0.37$ eV (2)

mechanism:

$CH_3CO_2 \rightarrow CO_2 + CH_3$ $\Delta_r H \sim -0.22$ eV (2a)

$CH_3 + CH_3CO_2H \rightarrow CH_4 + CH_3CO_2$ $\Delta_r H \sim -0.15$ eV (2b)

In the Na-doping method, the Na is ionised rather than the molecules in the cluster. The relatively low ionisation potential of Na prevents post-ionisation intracluster reactions and pronounced evaporation from occurring when using the Na-doping method. It leaves the original cluster/particle size distribution largely intact and provides a detailed size distribution, not only an average mean size. The Na-doping method allows the determination of size distributions over a broad range from clusters containing only a few molecules to

particles with sizes up to ~ 20 nm.[14, 15, 22, 23, 25] We are curently working towards a more quantitative understanding of the Na-doping method. All different processes indicated in Fig. 2 (Na-capture efficiency, Na-sticking efficiency, photoionisation efficiency, detection efficiency) contribute to the overall detection efficiency. As discussed in refs.[15, 25, 40] a detailed understanding of the size- and substance-dependence of the individual processes is required to turn Na-doping into a quantitative method.

3. Size-dependence of the ionisation energy and bandwidth

3.1. Photoemission from the HOMO of $(H_2O)_n$, $(NH_3)_n$, and $(CH_3OCH_3)_n$

Very few size-dependent photoemission studies exist for neutral molecular aggregates with sizes that reach into the nanometre range. To the best of our knowledge corresponding experimental data for the outer valence region are available only for water, ammonia, and dimethyl ether aggregates.[6, 7, 9, 11-15] The most prominent size-dependent effect in the PE spectra is the systematic shift of the ionisation energies (IE) (see original PE spectra in refs.[9, 14, 15]). Fig. 4 shows the shift ΔIE between the IEs of the aggregates and the monomer (ΔIE = IE(mon.)-IE(aggr.)) as a function of the average aggregate size for ionisation from the highest occupied molecular orbital (HOMO) (note that similar trends are also observed for other valence orbitals). These experimental ΔIE values correspond to the differences of the values for the electron binding energies (BE) measured at their respective band maxima, which approximately correspond to the vertical IE. ñ denotes the average number of molecules per aggregate. The HOMO corresponds to the oxygen or nitrogen lone pair ($1b_1$ for H_2O, $2b_1$ for CH_3OCH_3, and $3a_1$ for NH_3). The size-dependent data from our studies for $(NH_3)_n$, and

$(CH_3OCH_3)_n$ were recorded under the same experimental conditions with a VUV laser and VMI (scheme (ii) in section 2.1).[14, 15] In both studies, size distributions were measured independently of the photoemission spectra with the Na-doping method as described in section 2.2. The corresponding data for $(CH_3OCH_3)_n$, are indicated in Fig. 4 by empty (black) squares connected by a full (black) line while empty (blue) circles connected by the full (blue) line are used for the corresponding $(NH_3)_n$ data. An additional single value for $(NH_3)_n$ for ñ ~ 1600 has been reported in the synchrotron study of Lindblad *et al.*[12] and is indicated in Fig. 4 by the open (blue) circle that is not connected by the (blue) line. The particle size in this study was estimated with a scaling law. The data for $(H_2O)_n$ in Fig. 4 is a compilation from different synchrotron studies. The empty (red) triangles connected by a full (red) line are from ref.[9] while the other empty (red) triangles not connected by the line are values for single sizes from refs.[6, 7, 11, 13]. In all $(H_2O)_n$ studies, the average size was not determined experimentally but estimated from scaling laws. Although the uncertainty in size is seldom specified explicitly it seems to be significant, which makes size-dependent analyses difficult (see section 2.2).

The size-dependence of the HOMO IE can have its origin in different phenomena. The dominant factors are likely to be the change in the initial-state orbital energy due to size-dependent structural changes in the neutral state upon progressive condensation (assuming 'final-state' effects play a minor role for the vertical transition) and the change in polarisation screening of the positive charge in the final state with increasing size. A third factor that may become important for the size-dependence of larger aggregates is inelastic electron scattering within the particle. Depending on the eKE it limits the probing depth to different degrees. (For further details on the origin of IE shifts see discussions in refs.[9, 27, 28, 38, 41] and references therein). The first two factors are intimately connected with each other: Different structures and different numbers of molecules around the ionisation site result in different degrees of

polarisation screening. In the simplest polarisation model, the aggregate is regarded as a continuous dielectric sphere which is polarised by the formation of a positive charge upon ionisation. Assuming the charge in the centre of a finite dielectric spherical cluster of radius r_c, the associated change in IE is:[3,44]

$$\Delta IE = \frac{e^2}{8\pi\varepsilon_0}\left(1-\frac{1}{\varepsilon}\right)\left(\frac{1}{r}-\frac{1}{r_c}\right) \qquad (3)$$

where r is the size of the cavity surrounding the charge, and ε is the relative permittivity of the cluster material at frequencies appropriate to describe screening mechanisms in a photoionisation experiment. This results in a linear dependence of ΔIE as a function of $\tilde{n}^{-1/3}$. Pure polarisation screening models have been proven successful to describe size-dependent shifts of the IE for rare gas clusters for core orbital ionisation.[38, 42] These studies found distinct bands and IEs for atoms in the surface and for atoms in the interior of the aggregates, both exhibiting a comparatively simple size-dependence ($\tilde{n}^{-1/3}$ dependence for the interior as described by eq. (3)). For the ionisation of valence orbitals of molecular systems a more complicated size-dependence is expected because structural transitions are likely to occur with changing aggregate size, different spectral features may be unresolved (e.g. surface, bulk), and charge delocalisation effects in the final state may contribute,. Analysis with a simple polarisation model seems questionable in this case since it provides ambiguous results.

The ionisation from the HOMO of $(H_2O)_n$, $(NH_3)_n$, and $(CH_3OCH_3)_n$ results in a single more or less symmetric band in the PE spectra (see original publications). Therefore individual bands attributable to ionisation in the surface region or in the interior of the aggregate cannot be clearly distinguished in contrast to the rare gas clusters mentioned above. Furthermore, the IEs in Fig. 4 seem not to follow a simple ñ-dependence with increasing size, such as e. g. $\tilde{n}^{-1/3}$, and convergence to the values of the infinite bulk for $(H_2O)_n$, $(NH_3)_n$ for ñ

$\rightarrow \infty$ is also not obvious from Fig. 4b. Infinite bulk values for H_2O and NH_3 are indicated by filled (for liquid bulk) and half-filled (for solid bulk) triangles and circles at $\tilde{n}^{-1/3} = 0$, respectively.[41, 43, 44] To the best of our knowledge no bulk values for CH_3OCH_3 have been published yet. Barth et al. concluded from their data set for relatively small H_2O aggregates with sizes up to $\tilde{n} \sim 108$ (empty red triangles connected by the solid line in Fig. 4) that the IE energy converges with $\tilde{n}^{-1/3}$ to the liquid bulk value of water (filled triangle at $\Delta IE = 1.45$). However, if other published data for larger H_2O aggregates are also considered (empty (red) triangles not connected by the full line in Fig. 4) this conclusion seems questionable. These additional data points clearly show a deviation from a simple $\tilde{n}^{-1/3}$ polarisation screening behaviour. Furthermore, it seems more plausible to us that the H_2O aggregates formed in supersonic expansions are solid and not liquid, again speaking against convergence to the liquid bulk. We rather believe that the alleged $\tilde{n}^{-1/3}$-convergence to the liquid water value observed in ref.[9] is accidental and a result of the limited cluster size range studied. Like the H_2O aggregates, the NH_3 aggregates do not obey a $\tilde{n}^{-1/3}$ size-dependence either. Instead of trying to fit a polarisation screening model to the ammonia data we have taken a different approach in ref.[15]. We decided to compare our data with previous experimental results from infrared (IR) spectroscopy and calculated data for ionisation energies of NH_3 aggregates (covering the size range from the dimer to particles with up to 100 nm) with the goal to clarify whether our PE data are consistent with these previous findings refs.[45-53] For details of the argumentation we refer the reader to ref.[15]. Briefly, the size-dependence of the IE in Fig.4 is consistent with the size-dependence predicted from the combined molecular dynamics/quantum mechanics approach for liquid NH_3 aggregates in ref.[53]. This agreement implies that the aggregates we ionise have a predominantly amorphous structure. Furthermore, the IR studies predict all NH_3 aggregates investigated here (even the largest ones with ~ 7 nm in diameter or $\tilde{n} \sim 4700$) to be clearly dominated by their amorphous

surface layer rather than their crystalline core (surface fraction > 76%).[46, 48, 50] The combination of these two observations led us to the interpretation that the size-dependence of the IE for $(NH_3)_n$ in Fig. 4 comes from aggregates that are dominated by an amorphous surface layer with an average coordination number similar to that of the liquid.[15] This might not be the only possible explanation, but it is at least fully consistent with other independent studies.

The quality of the data currently available for neutral aggregates poses a major restriction on making a detailed data analysis. The uncertainties in band positions, band widths, and β-parameters are substantial, amongst other reasons due to limited signal/noise or lack of accurate size information. Furthermore, the number of data points as a function of size for a certain compound is still limited, in particular for very large aggregates (Fig. 4). Although this makes the comparison between the three systems $(H_2O)_n$, $(NH_3)_n$, and $(CH_3OCH_3)_n$ difficult at this point we would like to add here a few speculative remarks. Fig. 4a suggests that the IE for all three substances follows a common size-dependent trend: A pronounced decrease of the IE energy with increasing size for smaller clusters, which seems to level off for larger aggregates ("plateau formation"). Potential explanations[14, 15] for the plateau formation are: (i) Convergence to the infinite bulk is reached. (ii) Structural convergence within a certain size-range is reached. (iii) The probing depth is limited because the electron escape length is reached. (iv) The plateau is not real, but a measurement artefact. Assuming that (iv) can be excluded, we currently believe a combination of (ii) and (iii) to be the most likely explanation. This hypothesis is speculative and its evaluation must await future experimental data of improved quality in particular extending to larger particle sizes than the ones presently observed.

For completeness, we list in Table 1 the size-dependent bandwidths (full widths at half maximum, FWHM) for $(H_2O)_n$, $(NH_3)_n$, and $(CH_3OCH_3)_n$. As expected, the bandwidths

increase with increasing aggregate size for all three substances. The broadening between the monomer and the largest clusters varies substantially, between a factor of ~2 for NH_3 and afactor of >4 for H_2O. A general broadening with increasing size is expected due to the interaction between the orbitals of neighbouring molecules and the broader variety of different structural motifs that can be realised. The course of the broadening with increasing size, however, seems to be quite different for the water aggregates compared with the dimethyl ether aggregates. $(H_2O)_n$ aggregates are reported to reach the liquid bulk value and thus a "plateau" value already for clusters that consist of less than ~8 molecules.[9] The widths for $(CH_3OCH_3)_n$, by contrast, converge much more slowly.[14] They seem to reach a plateau only for aggregates with a few hundred molecules. The behaviour of $(NH_3)_n$ is somewhere in between. As discussed in ref.[14], this might be a consequence of the different degree of hydrogen-bonding in the three compounds. Another aspect worth mentioning in this context is the potential influence of the fast intermolecular proton transfer (equivalent to Eq. (1)) that occurs upon ionisation in all three systems.

3.2. Photoemission from the HOMO of $Na(CH_3OH)_n$

Solvation phenomena and properties of solutions are of key importance for the understanding of chemical processes. Insight into the molecular details of solvation phenomena can be gained from studies of nanoscale solvent/solute systems and their evolution towards the bulk. In principle, angle-resolved photoelectron spectroscopy provides a way to probe the change in orbital character (hybridisation) of a solute in nanosized solvent droplets/particles of varying size. However, apart from our studies on nano-solutions of a sodium atom in methanol, water, ammonia, and dimethyl ether aggregates (present study and forthcoming publications), which seem to be the first to provide information on the PAD

(section 4.1), only one more study is known to us that used photoelectron spectroscopy to characterise neutral nano-solutions.[13] More but still limited data is available for surface/bulk solutions from photoelectron studies on liquid microjets[27, 54] (and references therein).

The evolution of the ionisation energy of $Na(CH_3OH)_n$, $Na(CH_3CH_2OH)_n$, $Na(H_2O)_n$, and $Na(NH_3)_n$ over a broad size range from small clusters to large aggregates was extensively studied in the groups of Buck and Hertel.[24, 55] The results of this pioneering work were very recently reviewed in ref.[24]. These investigations are mostly based on photoionisation mass spectroscopy; i. e. the appearance energy (AE) of a certain cluster size is determined from the mass spectrum recorded as a function of the photon energy and then used as measure of the IE. The size-dependence of the AE was found to depend on the type of solvent. For methanol, ethanol, and water, the AE drops continuously up to n = 6, 6, and 4, respectively, and levels off for higher n at approximately the values of the liquid bulk solutions (see Fig. 5a which shows as an example the evolution of the AE for $Na(CH_3OH)_n$). $Na(H_2O)_n$ exhibits a more complicated behaviour than the alcohols due to the presence of two different isomers, while the behaviour of $Na(NH_3)_n$ is qualitatively different.[24] Its AE decreases gradually with the number of solvent molecules (approximately linear as a function of $n^{-1/3}$) and reaches an extrapolated value of only 1.66 eV ($n\rightarrow\infty$) close to the liquid bulk value for the solvated electron. The size-dependence of the AE seems to result from a delicate balance of the distance between the counterion and the "solvated" electron distribution, the location of the electron distribution (surface, interior), the compactness of the electron distribution, and the expansion conditions resulting in the formation of different isomers.[24] Although we cannot cover this subject fully, we would also like to refer the reader to cluster and liquid microjet studies that address reactive processes in Na-solutions (see ref.[56] and references therein).

We have recently started to use angle-resolved photoelectron spectroscopy as an alternative method to study the evolution of the IE and the electron distribution of

$Na(CH_3OH)_n$, $Na(H_2O)_n$, $Na(CH_3OCH_3)_n$, and $Na(NH_3)_n$ nano-solutions. In particular the angular information potentially provides additional insight into the question of electron location and distribution. For the present review, we limit ourselves to a brief comparison of the size-dependent IEs of $Na(CH_3OH)_n$ with previous data available from photoionisation mass spectrometry[57] (see Fig. 5a) and to the publication of β-parameters for the ionisation from the respective HOMOs (section 4.1). Data for the other solvents (H_2O, CH_3OCH_3, and NH_3) and in particular the comparison between the different nano-solutions will be the subject of forthcoming publications.

We have recorded photoemission spectra for a series of different $Na(CH_3OH)_n$ aggregate sizes with ñ ranging from 1 to 32 and n_{max} ranging from 1 to ~109 (see Table 2). (ñ is the count mean and n_{max} is the maximal number of solvent molecules observed for a certain aggregate distribution, respectively). Fig. 5b and c show as an example the photoelectron spectrum of a cluster distribution with high monomer and dimer contribution and the corresponding cluster distribution obtained from the ion mass spectrum. Two different types of IE were extracted from Lorentzian line fits (representing different cluster sizes) to the photoelectron spectra: Values at the Lorentzian band maxima (IE) and threshold values (IE_t) determined at the low binding energy side of the Lorentzians where the electron signal was twice the noise. The AEs and IEs are depicted in Fig. 5a as a function of $n^{-1/3}$ or $ñ^{-1/3}$ and the IE_t as a function of $n_{max}^{-1/3}$. The evolution of the IEs determined from photoemission agree well with the ones observed for the AEs in ref. [57]. The IE and AE decrease pronouncedly for the first few solvent molecules and then level off. The plateau value of the IE for larger clusters is somewhat higher than the corresponding value for the AE. This is not surprising since the two measurement techniques are not equivalent. The plateau value of our IE lies close to the corresponding value recently determined for "solvated electrons" in liquid microjet photoemission studies of NaI/methanol solutions in ref.[58], depicted in Fig. 5a as a

red dot at $N^{-1/3} = 0$. More surprising than the evolution of the IE is the size-dependence of the IE_t. It continues to decrease for larger solvent aggregates and seems to approach the threshold values of the NaI/methanol bulk study (blue square at $n^{-1/3} = 0$). We have also performed ab initio calculations for the vertical and the adiabatic IE for clusters with up to 15 solvent molecules. These calculations also find a plateau for the vertical IE (approximately equivalent to the IE in Fig. 5a) and a decrease of the adiabatic IE (~IE_t) at larger cluster sizes, which seems to be consistent with the current observations. The calculations also imply that the different behaviour of the adiabatic and the vertical IE comes from the major reorganisation of the hydrogen-bond network upon ionisation.

4. Size-dependence of the β-parameter

The emphasis of the present mini-review is devoted to angle-dependent information on photoelectrons. For neutral molecular aggregates, the corresponding data available is very sparse. To the best of our knowledge it is limited to the β-parameters listed in Tables 1 and 2, from refs.[11, 14, 15] and from the present work. Substantially more data than for neutral molecular aggregates exist for neutral rare gas aggregates[10, 19] as well as for anionic clusters[1-4] (and references therein). Angular information is often provided by a single parameter which is referred to as the "asymmetry parameter", "anisotropy parameter" or "β-parameter". The PAD of a randomly oriented sample for single photon ionisation by linearly polarised light assuming that the dipole approximation and the central potential approximation apply is given by Eq. (4)[59]:

$$\frac{d\sigma}{d\Omega} = \frac{\sigma_{tot}}{4\pi}\left[1 + \beta(eKE)\frac{1}{2}\left(3\cos^2\theta - 1\right)\right] \quad (4a)$$

$$\beta = \frac{l(l-1)R_{l-1}^2+(l+1)(l+2)R_{l+1}^2-6l(l+1)R_{l-1}R_{l+1}\cos(\delta_{l+1}\delta_{l-1})}{(2l+1)[lR_{l-1}^2+(l+1)R_{l+1}^2]} \quad (4b)$$

Where $\frac{d\sigma}{d\Omega}$ and σ_{tot} are the differential and the total photoemission cross section, respectively. *eKE* is the photoelectron kinetic energy and θ is the angle between the photoelectron velocity vector and the polarisation axis of the incident light. l is the electron angular momentum quantum number and $R_{l\pm1}$ and $\delta_{l\pm1}$ are the radial dipole matrix elements and the phase shifts, respectively, of the two scattered partial waves with $l \pm 1$. The values of β are restricted to the range between -1 and 2. It is 0 for completely isotropic photoemission. Positive and negative values of β indicate that the photoelectrons are preferentially ejected parallel and perpendicular with respect to the polarisation axis of the light. β depends on the orbital angular momentum of the initial state, the radial dipole matrix elements and the phase shifts of the two scattered partial waves (Eq. 4b), and for larger aggregates on elastic and inelastic intracluster electron scattering [8, 10, 11, 14-16, 19-21] The last three factors depend markedly on eKE. Together with the change in the orbital character (hybridisation) with increasing aggregate size this is expected to result in a complicated size- and energy-dependence of the asymmetry parameter. In the following, we discuss the size-dependence of the β-parameter for aggregates that consist of a single substance (self-solvation) and for a solute (Na) dissolved in an aggregate of varying size.

4.1. Size/solvation-dependence of the β-parameter

One of the essential questions to address for molecular aggregates is: how much of the size-dependence of β is due to the change in the orbital character caused by subsequent condensation and how much comes from intracluster electron scattering? Size-dependent studies for neutral rare gas aggregates containing up to several thousand atoms per cluster

reveal a general trend towards more isotropic photoelectron distributions for larger aggregates.[8, 10, 16, 19-21] This observation was mainly traced back to elastic electron scattering within the aggregate, which randomises the emission direction of the photoelectrons resulting in lower values of the β-parameter. However, possible contributions from changes in the orbital character due to clustering and from surface/bulk excitations were also discussed. A general conclusion on the relative importance of orbital-specific and scattering-specific effects seems not to have been reached yet. For molecular systems, truly size-dependent studies in the valence region are limited to $(CH_3OCH_3)_n$[14],$(NH_3)_n$[15], and Na-doped clusters of H_2O, CH_3OH, CH_3OCH_3, and NH_3 (present study and manuscripts in preparation).

As Table 1 reveals, $(CH_3OCH_3)_n$ is not a very instructive case in this context since the photoemission of CH_3OCH_3 gas phase monomer is essentially isotropic and remains so for larger clusters within the experimental uncertainty. For $(NH_3)_n$ by contrast, photoemission becomes quickly more isotropic with increasing aggregate size (Table 1) similar to the behaviour found for rare gas clusters. At this point, it is unclear whether the lowering of β is dominated by changes in the orbital character or by electron scattering or whether both factors contribute. Electron scattering in a particle certainly randomises the angular distribution of the photoemission. However, the lowering of β for $(NH_3)_n$ is observed for relatively small clusters for which elastic scattering should not yet be so important. To clarify potential orbital-specific contributions, we have performed a natural atomic orbital (NAO) analysis based on B3LYP/6-311+G** ab initio calculations for the n highest molecular orbitals for $(NH_3)_n$ clusters with $n \leq 5$. Following the simple model suggested in refs.[60, 61] we have then calculated averaged β-parameters for these small clusters (see more details further below). Table 1 lists the corresponding values (referred to as "this work") that are obtained if the p-NAO contributions are assumed to give rise to a pure d partial wave. At least within this extremely simple model, an orbital specific contribution cannot be confirmed clearly at this

point. Corresponding size-dependent studies of β for $(H_2O)_n$ aggregates are still missing. Currently, only values for two approximate sizes with ~58 and ~84 molecules are available for water aggregates as indicted in Table 3.[11] A pronounced decrease of β compared with the monomer value is also observed in this case. Using a simple scattering model, the authors attribute most of the lowering of β to the randomisation by elastic electron scattering within the cluster. However, they also provide first evidence for an additional small orbital-dependent contribution.

The dependence of the anisotropy parameter on the degree of solvation for a solute in a cluster of varying size is demonstrated here for the example of Na atoms in $(CH_3OH)_n$ aggregates (section 3.2). To the best of our knowledge this is the first report of angle-resolved data for neutral solute/solvent aggregates. Table 2 lists experimental and calculated β-parameters for the HOMO of $Na(CH_3OH)_n$ as a function of the number of methanol solvent molecules. The experimental data show a trend towards more isotropic photoemission with increasing size (for ionisation with 4.66 eV photons). A natural atomic orbital (NAO) analysis of MP2/6-311+G** ab initio calculations suggest that this trend in β is due at least in part to an increase in the p-orbital contribution to the HOMO as solvation proceeds. According to this analysis, the p-orbital contribution is predicted to increase from 5% for $Na(CH_3OH)$ to 35% for $Na(CH_3OH)_5$. To estimate the influence of such an increase in the p-character on the photoemission anisotropy, we have calculated limiting values for β-parameters following the procedure suggested in refs.[60, 61] and assuming that Eq. (4) is valid. β_{int} is the limiting value obtained when conferring total interference (β = -1) and β_s and β_d are the limiting values for emission of a pure s and a pure d partial wave, respectively, from the p-fraction of the orbital. Note that the dominating s-fraction of the orbital always emits a p-partial wave. Although the absolute β-values slightly differ for the three limiting cases the trend towards lower β-values for larger clusters seems robust, suggesting that the

experimentally observed trend indeed arises from changing orbital character/hybridisation with increasing solvation (detailed data to be published elsewhere). The deviations between the absolute experimental and calculated β-values in Table 2 are pronounced. Experimental artefacts as described in section 4.2 could contribute to this deviation. Another factor is certainly the simple approximate model used to predict β, which is based on assumptions that may not apply (e. g., central potential assumption, atomic selection rule for partial waves, no explicit treatment of dynamical electron-energy dependent effects). This raises the general issue of proper modelling of β-parameters for molecular aggregates, which is essential to clarify the importance of orbital-specific and scattering-specific contributions in combination with experimental results. In general, this constitutes a difficult task and no general broadly applicable strategy seems to be available yet. We refer here to corresponding discussions for anion clusters in refs.[1, 2, 4, 17, 60-62].

4.2 Artefacts in β-parameter measurements

Various experimental factors can influence and thus falsify the measured value of the β-parameter. Several of them are dependent on the specific experimental setup. To detect potential artefacts, reference measurements of a system with a well-known asymmetry parameter are usually performed under experimental conditions that mimic those of the system for which β has yet to be determined. In the cluster studies discussed above either photoelectrons from H_2O monomer[11] or xenon atoms[14, 15] recorded under similar conditions were used as a reference. However, the amount of reference data available is limited such that it is not always possible to find corresponding data. For the $Na(CH_3OH)_n$ studies, for example, we could not perform reference measurements with the same laser (266nm YAG) but had to rely on photoelectron measurements of Xe atoms recorded with the VUV laser

system described in section 2.1. The intention of this subsection is to provide an overview of potential artefacts in β-parameter measurements and their magnitude for a typical VMI setup.

Distortion of the photoelectron trajectories can arise from insufficient shielding of electric and magnetic fields in the photoelectron spectrometer or from the formation of too many charges in the ionisation volume (space charging). Electric and magnetic stray fields are typically minimised by insertion of additional shielding electrodes[17] and by using a mu-metal tube that covers the entire inside of the spectrometer (see Fig. 1), respectively. The formation of high charge densities in the ionisation volume can be avoided by reduction of the laser fluence and/or the sample density. The influence of laser fluence on the β-parameter of $Na(CH_3OCH_3)_3$ is shown in Fig. 6. An increase in the laser fluence increases the local charge density in the ionisation volume which produces a PAD that is increasingly isotropic (until $\beta = 0$). This is a well-known artefact in angle-resolved photoelectron spectroscopy. Pulsed laser experiments are particularly prone to this artefact. As demonstrated in Fig. 6, the influence on β can be huge for pulsed systems. Systematic studies of signal dependence on fluence and absorber concentration are required to determine proper experimental conditions.

The influence of incompletely shielded electric and magnetic fields and of imperfections in VMI optics is usually less pronounced but not necessarily negligible. To demonstrate this point, we have simulated raw images with SIMION[63] for a single photoelectron band with a defined initial energy spread and an initial energy-independent β-value of 1.2 (to match with our experimental finding for photoionisation to the $^2P_{1/2}$ of Xe with a 17.5 eV photon), once for the ideal case (no distortion of image, referred to as "round" image) and once for a case with a slightly distorted image (referred to as "eccentric" image). The assumed distortion results in a marginal elliptical eccentricity in the raw image which corresponds to a difference in the image radius between vertical and horizontal detector axis of only 1-2 pixels. To determine β, the simulated raw images were then reconstructed with BASEX. The resulting

energy dependent β-parameters across the photoelectron band are plotted in Fig. 7. Although the values of β averaged across the entire band (FWHM) are similar and close to the correct value of 1.2 (β = +1.18±0.24 for the round image and β = +1.21±0.57 for the eccentric image) the alleged energy-dependence of β for the distorted case (decreasing β with increasing image radius in Fig. 7) is simply an artefact of the image eccentricity. This type of artefact will always be a problem when image distortion is on a similar scale to the peak widths in the speed distribution.

A further type of artefact can be caused by inhomogeneities of the electron detection at the MCP/phosphor screen imaging detector.[64] The top image in Fig. 8 shows an experimental raw image that suffers from detection inhomogeneities causing asymmetries in the image (referred to as "non-centroided") that violate the cylindrical symmetry (section 2.1) - clearly an artefact. The lower image is for an identical sample but recorded with centroiding, which balances the inhomogeneities (referred to as "centroided").[65] Table 3 lists the β-parameters extracted from the non-centroided and centroided image, respectively. β_{tot} denotes the value that is extracted using the entire image while β_{left} and β_{right} correspond to values for which only the left and right part of the images were used for reconstruction. This list clearly demonstrates that β_{tot} for the non-centroided image is falsified because of the strong differences between β_{left} and β_{right}. The values of β for the centroided image, by contrast, are all very similar; i. e. $\beta_{tot} \approx \beta_{left} \approx \beta_{right}$, as it should be.

The last factor we would like to mention here is the image reconstruction method itself, which can also cause deviations from the correct β value. This aspect has been investigated in ref.[17]. For that purpose, noise-free as well as noisy raw images with defined input β-parameters were simulated and then reconstructed using different reconstruction methods (BASEX, pBASEX, and a new algorithm suggested by the authors in ref.[17]). The β-parameters extracted from reconstruction were then compared to the input (correct) β-

parameters. In particular for BASEX, overly isotropic β-values were found (up to deviations of 0.5 for the noisy case) while the new algorithm reproduced the input values almost correctly. We have repeated a similar comparison with BASEX and p-BASEX but could not confirm substantial deviations between the two reconstruction programs.

It is difficult to quantify the general influence of artefacts on the β-parameters. However, the above examples clearly demonstrate that deviations from the correct values can be very substantial, i.e. on the order of 0.5 or even more. Although this need not be true for all cases, many artefacts rather seem to lower rather than increase the values of β, i.e. they make the perceived angular distributions of the photoelectrons more isotropic. This is probably because in many cases the artefacts tend to be of "random character".

5. Concluding Remarks

This mini-review summarises results in an emerging branch of PE spectroscopy: The study of PADs of neutral molecular aggregates as a function of aggregate size with the goal to develop a clearer understanding of condensation and solvation phenomena. First trends seem to crystallise from the very limited experimental data available to date, such as the formation of plateau values for IEs and β-parameters above a certain aggregate size. Such effects might be of structural origin or arise from intracluster electron scattering processes.

More data of higher quality and in particular covering a broader size range are required to further explore such trends. On the experimental side, there are two major challenges. First, there is the development of an experimental method that would allow size-selection of neutral nanosized aggregates before the actual photoemission experiment. Second, would be the

reduction of the influence of artefacts in PAD measurements. The question of how well one can disentangle the different contributions to shifts in IEs and changes in β-parameters will be crucial for advancement of the field. This particularly concerns the relative contributions of orbital character versus intracluster electron scattering. Here, further development on the modelling side will be needed together with an extension of the experimental methods, for example towards time-resolved photoemission studies.

ACKNOWLEDGMENT

We are very grateful to David Stapfer and Markus Kerellaj from the LPC machine shop, and to Markus Steger from the LPC electronic shop for their competent and diligent assistance in the realisation of the experimental setup. We would also like to thank Prof. Suits and his group for providing us with the NuAcq software and Dr. David Luckhaus for his support with the ab initio calculations. Financial support was provided by the ETH Zürich and the Swiss National Science Foundation under project no. 200021_146368.

LIST OF FIGURES

Figure 1. Drawing of our photoelectron imaging spectrometer with the VUV and UV laser light sources indicated. The experimental setup consisting of the source chamber (A), the Na-oven chamber (B), the ionisation/detection chamber (C), the four-wave mixing chamber (D) and the diffraction grating chamber (E). Details given in text.

Figure 2. Sketch of the Na-doping method. The four main steps are highlighted: Na-capture, Na-sticking, photoionisation, and detection. (R, E, and G denote the repeller, extractor and ground plate, respectively.)

Figure 3. Mass spectra of a given acetic acid cluster distribution. Upper panel: clusters ionised via the Na-doping method. Lower panel: the same cluster distribution ionised by VUV radiation with 13.3 eV photon energy.

Figure 4. ΔIE (= IE(monomer) – IE(aggregate)) of the HOMO as a function of size $\tilde{n}^{-1/3}$ for $(H_2O)_n$, $(NH_3)_n$, and $(CH_3OCH_3)_n$. (a) and (b):The empty black squares indicate $(CH_3OCH_3)_n$ data, empty red triangles indicate $(H_2O)_n$ data, empty blue circles indicate $(NH_3)_n$ data. (b): Infinite bulk values for H_2O and NH_3 are indicated by filled (liquid bulk) and half-filled (solid bulk) triangles and circles at $\tilde{n}^{-1/3} = 0$, respectively. See text for data references.

Figure 5. a) Comparison of ionisation energies for the HOMO of $Na(CH_3OH)_n$ as a function of size ($N^{-1/3}$) between appearance energies (AE) found by Dauster *et al.*[57] (black bars) and values of band maxima (IE) (empty red circles) and threshold values (IE_t) (empty blue squares) determined in the present work. N denotes either n, $\tilde{n}$ or n_{max} and E denotes AE, IE or IE_t (see text). Typical error bars for the IE and IE_t are < 80 meV. The solid red circle and blue square are measured values for the IE and IE_t, respectively, of a solvated electron in bulk liquid methanol.[58] b) An example photoelectron spectrum of $Na(CH_3OH)_n$ with $n \leq 11$. c) Mass spectrum of $Na(CH_3OH)_n$ clusters that corresponds to the photoelectron spectrum shown in b).

Figure 6: Variation of β as a function of average laser fluence for photoemission from $Na(CH_3OCH_3)_3$ ionised with 4.66 eV light. The laser beam waist at the ionisation

point was 1.3 mm (half-width $1/e^2$) for all data points except the highest fluence shown, where it was 0.3 mm.

Figure 7: Variation in anisotropy across a peak in the speed distribution of a simulated image with $\beta = +1.2$. The speed distribution and corresponding β-values of a 'round' image are depicted by the black dot-dashed and solid traces, respectively. The speed distribution and corresponding β-values of an 'eccentric' image are depicted by the red dashed and solid traces, respectively. The radius of the 'eccentric' image was elongated by 2 pixels. BASEX was used for image reconstruction.

Figure 8: Raw photoelectron images of $Na(CH_3OH)_n$ ($n<12$) collected without (top) and with centroiding (bottom). The double-headed arrows denote the electric field polarisation axis of the incoming 4.66 eV radiation used for ionisation. Electron intensity increases from black to blue to red to yellow. Absolute colour scales are different for the two images.

TABLES

Table 1. Measured bandwidths (FWHM) and β-parameters as a function of size for the HOMO of $(H_2O)_n$, $(NH_3)_n$, and $(CH_3OCH_3)_n$ for indicated photon energies.

Substance	ñ	FWHM (eV)	β-parameter @ photon energy
$(H_2O)_n$	1	0.30(1) [41]	+1.31(3) @ 30.0 eV [66]
			+1.4 @ 38.7 eV [29]
			+1.38(8) @ 40 eV [11]
			+1.48(3) @ 42.7 eV [66]
			+1.59(8) @ 60 eV [11]
			+1.53(4) @ 60.3 eV [66]
	>6-8	similar to ∞_{liquid} [6, 9]	-
	58	-	+0.83(8) @ 40 eV [11]
	84	-	+1.17(8) @ 60 eV [11]
	∞_{liquid}	1.45(8) [41]	+0.8 @ 38.7 eV [29]
	∞_{ice}	1.28/1.3 [41]	-
$(NH_3)_n$	1	0.93±0.1 [15]	+1.10±0.62 @ 13.318 eV [15]
			+1.42(2) @ 30 eV [67]
			+1.48(2) @ 40 eV [67]
			+1.59(2) @ 60 eV [67]
			+1.08 [this work]
	2		+1.08 [this work]
	3		+1.07 [this work]
	4		+1.12 [this work]
	5		+1.08 [this work]
	6	1.64±0.3 [15]	-
	10	1.75±0.2 [15]	+0.15±0.42 @ 13.318 eV [15]
	24	1.43±0.2 [15]	+0.17±0.49 @ 13.318 eV [15]
	27	2.28±0.2 [15]	+0.12±0.29 @ 13.318 eV [15]
	281	1.84±0.1 [15]	+0.21±0.17 @ 13.318 eV [15]
	1600	1.8 [12]	-
	2276	1.95±0.1 [15]	+0.18±0.12 @ 13.318 eV [15]

	∞_{ice}	1.8 [43]	-
$(CH_3OCH_3)_n$	1	0.46±0.10 [14]	-0.11±0.19 @ 13.318 eV [14]
	3	0.97±0.09 [14]	-
	28	1.02±0.21 [14]	similar to value for ñ = 1441
	70	0.98±0.12 [14]	similar to value for ñ = 1441
	713	1.37±0.18 [14]	similar to value for ñ = 1441
	1441	1.49±0.21 [14]	-0.08±0.15 @ 13.318 eV [14]

Table 2. Experimental (β_{exp}) and calculated (β_{int}, β_s, β_d) β-parameters as a function of size for the HOMO of $Na(CH_3OH)_n$. n, ñ, n_{max} denote the number of solvent molecules per cluster, the average number of solvent molecules per cluster, and the number of solvent molecules in the largest aggregate observed in each size distribution, respectively. Typical uncertainty in the experimentally determined β-parameters is ±0.2.

	n	β_{exp}	β_{int}	β_s	β_d
	0	-	2	2	2
	1	0.71	1.86	1.90	1.95
	2	0.65	1.80	1.87	1.93
	3	-	1.76	1.84	1.92
	4	-	1.19	1.46	1.73
	5	-	0.96	1.31	1.65
n_{max}	ñ				
11	6	0.41			
25	9	0.37			
43	15	0.30			
69	24	0.24			
109	32	0.19			

Table 3. Experimental β-parameters for the HOMO of $Na(CH_3OH)_n$ extracted from the inhomogeneous (top) and the homogeneous (bottom) images in Fig. 8. Uncertainty in the reported β-parameters is ±0.25 for both cases.

N	non-centroided image			centroided image		
	β_{tot}	β_{left}	β_{right}	β_{tot}	β_{left}	β_{right}
1	0.66	0.54	0.82	0.72	0.72	0.73
2	0.55	0.44	0.69	0.65	0.66	0.64
<6>	0.33	0.22	0.45	0.40	0.43	0.38

REFERENCES

1. C. Bartels, C. Hock, J. Huwer, R. Kuhnen, J. Schwöbel and B. von Issendorff, *Science*, 2009, **323**, 1323.
2. E. R. Grumbling and A. Sanov, *J. Chem. Phys.*, 2011, **135**, 164301.
3. R. M. Young and D. M. Neumark, *Chem. Rev.*, 2012, **112**, 5553.
4. J. J. Melko and A. W. Castleman, Jr., *Phys. Chem. Chem. Phys.*, 2013, **15**, 3173.
5. A. Sanov and R. Mabbs, *Int. Rev. Phys. Chem.*, 2008, **27**, 53.
6. O. Björneholm, F. Federmann, S. Kakar and T. Möller, *J. Chem. Phys.*, 1999, **111**, 546.
7. G. Öhrwall, R. F. Fink, M. Tchaplyguine, L. Ojamäe, M. Lundwall, R. R. T. Marinho, A. N. de Brito, S. L. Sorensen, M. Gisselbrecht, R. Feifel, T. Rander, A. Lindblad, J. Schulz, L. J. Sæthre, N. Mårtensson, S. Svensson and O. Björneholm, *J. Chem. Phys.*, 2005, **123**, 054310.
8. D. Rolles, Z. D. Pešic, H. Zhang, R. C. Bilodeau, J. D. Bozek and N. Berrah, in *XXV International Conference on Photonic, Electronic and Atomic Collisions*, eds. U. Becker, R. Moshammer, P. Mokler and J. Ullrich, 2007, vol. 88, p. 012003.
9. S. Barth, M. Ončák, V. Ulrich, M. Mucke, T. Lischke, P. Slavíček and U. Hergenhahn, *J. Phys. Chem. A*, 2009, **113**, 13519.
10. H. Zhang, D. Rolles, J. D. Bozek and N. Berrah, *J. Phys. B*, 2009, **42**, 105103.
11. C. Zhang, T. Andersson, M. Förstel, M. Mucke, T. Arion, M. Tchaplyguine, O. Björneholm and U. Hergenhahn, *J. Chem. Phys.*, 2013, **138**, 234306.
12. A. Lindblad, H. Bergersen, W. Pokapanich, M. Tchaplyguine, G. Öhrwall and O. Björneholm, *Phys. Chem. Chem. Phys.*, 2009, **11**, 1758.
13. L. Partanen, M.-H. Mikkelä, M. Huttula, M. Tchaplyguine, C. Zhang, T. Andersson and O. Björneholm, *J. Chem. Phys.*, 2013, **138**, 044301.
14. B. L. Yoder, A. H. C. West, B. Schläppi, E. Chasovskikh and R. Signorell, *J. Chem. Phys.*, 2013, **138**, 044202.
15. A. H. C. West, B. L. Yoder and R. Signorell, *J. Phys. Chem. A*, 2013, **Article ASAP**.
16. G. Öhrwall, M. Tchaplyguine, M. Gisselbrecht, M. Lundwall, R. Feifel, T. Rander, J. Schulz, R. R. T. Marinho, A. Lindgren, S. L. Sorensen, S. Svensson and O. Björneholm, *J. Phys. B*, 2003, **36**, 3937.
17. C. Bartels, Ph.D. theis, Albert-Ludwigs-Universität, 2008.
18. J. E. Mann, S. E. Waller and C. C. Jarrold, *J. Chem. Phys.*, 2012, **137**, 044301.
19. D. Rolles, H. Zhang, Z. D. Pešic, R. C. Bilodeau, A. Wills, E. Kukk, B. S. Rude, G. D. Ackerman, J. D. Bozek, R. D. Muiño, F. J. García de Abajo and N. Berrah, *Phys. Rev. A*, 2007, **75**, 031201.
20. H. Zhang, D. Rolles, Z. D. Pešic, J. D. Bozek and N. Berrah, *Phys. Rev. A*, 2008, **78**, 063201.
21. D. Rolles, H. Zhang, Z. D. Pešic, J. D. Bozek and N. Berrah, *Chem. Phys. Lett.*, 2009, **468**, 148.
22. S. Schütte and U. Buck, *Int. J. Mass Spec.*, 2002, **220**, 183.
23. C. Bobbert, S. Schütte, C. Steinbach and U. Buck, *Euro. Phys. J. D*, 2002, **19**, 183.
24. T. Zeuch and U. Buck, *Chem. Phys. Lett.*, 2013, **579**, 1.
25. B. L. Yoder, J. H. Litman, P. W. Forysinski, J. L. Corbett and R. Signorell, *J. Phys. Chem. Lett.*, 2011, **2**, 2623.
26. J. H. Litman, B. L. Yoder, B. Schläppi and R. Signorell, *Phys. Chem. Chem. Phys.*, 2013, **15**, 940.
27. B. Winter and M. Faubel, *Chem. Rev.*, 2006, **106**, 1176.

28. O. Link, E. Lugovoy, K. Siefermann, Y. Liu, M. Faubel and B. Abel, *Appl. Phys. A*, 2009, **96**, 117.
29. M. Faubel, K. R. Siefermann, Y. Liu and B. Abel, *Acc. Chem. Res.*, 2012, **45**, 120.
30. S. Thürmer, R. Seidel, M. Faubel, W. Eberhardt, J. C. Hemminger, S. E. Bradforth and B. Winter, *Phys. Rev. Let.*, 2013, **111**, 3005.
31. A. T. J. B. Eppink and D. H. Parker, *Rev. Sci. Instrum.*, 1997, **68**, 3477.
32. P. W. Forysinski, P. Zielke, D. Luckhaus and R. Signorell, *Phys. Chem. Chem. Phys.*, 2010, **12**, 3121.
33. C. J. Dasch, *Appl. Optics*, 1992, **31**, 1146.
34. V. Dribinski, A. Ossadtchi, V. A. Mandelshtam and H. Reisler, *Rev. Sci. Instrum.*, 2002, **73**, 2634.
35. G. A. Garcia, L. Nahon and I. Powis, *Rev. Sci. Instrum.*, 2004, **75**, 4989.
36. O. F. Hagena, *Surf. Sci.*, 1981, **106**, 101.
37. A. A. Vostrikov and D. Y. Dubov, *Zeit. Phys. D*, 1991, **20**, 429.
38. O. Björneholm, F. Federmann, F. Fössing, T. Möller and P. Stampfli, *J. Chem. Phys.*, 1996, **104**, 1846.
39. C. Steinbach, P. Andersson, J. K. Kazimirski, U. Buck, V. Buch and T. A. Beu, *J. Phys. Chem. A*, 2004, **108**, 6165.
40. P. W. Forysinski, P. Zielke, D. Luckhaus, J. Corbett and R. Signorell, *J. Chem. Phys.*, 2011, **134**, 094314.
41. B. Winter, R. Weber, W. Widdra, M. Dittmar, M. Faubel and I. V. Hertel, *J. Phys. Chem. A*, 2004, **108**, 2625.
42. O. Björneholm, F. Federmann, F. Fössing and T. Möller, *Phys. Rev. Let.*, 1995, **74**, 3017.
43. M. J. Campbell, J. Liesegang, J. D. Riley and J. G. Jenkin, *J. Phys. C*, 1982, **15**, 2549.
44. K. Y. Yu, J. C. McMenamin and W. E. Spicer, *J. Vac. Sci. Tech.*, 1975, **12**, 286.
45. T. A. Beu and U. Buck, *J. Chem. Phys.*, 2001, **114**, 7848.
46. M. Jetzki, A. Bonnamy and R. Signorell, *J. Chem. Phys.*, 2004, **120**, 11775.
47. M. N. Slipchenko, K. E. Kuyanov, B. G. Sartakov and A. F. Vilesov, *J. Chem. Phys.*, 2006, **124**, 241101.
48. C. Steinbach, U. Buck and T. A. Beu, *J. Chem. Phys.*, 2006, **125**, 133403.
49. M. N. Slipchenko, B. G. Sartakov and A. F. Vilesov, *J. Chem. Phys.*, 2008, **128**, 134509.
50. G. Firanescu, D. Luckhaus and R. Signorell, *J. Chem. Phys.*, 2006, **125**, 144501.
51. Y. Matsumoto and K. Honma, *Chem. Phys. Lett.*, 2010, **490**, 9.
52. W. Kamke, R. Herrmann, Z. Wang and I. V. Hertel, *Zeit. Phys. D*, 1988, **10**, 491.
53. T. S. Almeida, K. Coutinho, B. J. C. Cabral and S. Canuto, *J. Chem. Phys.*, 2008, **128**, 014506.
54. R. Seidel, S. Thuermer and B. Winter, *J. Phys. Chem. Lett.*, 2011, **2**, 633.
55. C. P. Schulz, R. Haugstätter, H. U. Tittes and I. V. Hertel, *Phys. Rev. Let.*, 1986, **57**, 1703.
56. W. A. Alexander, J. P. Wiens, T. K. Minton and G. M. Nathanson, *Science*, 2012, **335**, 1072.
57. I. Dauster, M. A. Suhm, U. Buck and T. Zeuch, *Phys. Chem. Chem. Phys.*, 2008, **10**, 83.
58. T. Horio, H. Shen, S. Adachi and T. Suzuki, *Chem. Phys. Lett.*, 2012, **535**, 12.
59. J. Cooper and R. N. Zare, *J. Chem. Phys.*, 1968, **48**, 942.
60. S. J. Peppernick, K. D. D. Gunaratne and A. W. Castleman, Jr., *Proc. Nat. Acad. Sci. USA*, 2010, **107**, 975.

61. S. J. Peppernick, K. D. D. Gunaratne, S. G. Sayres and A. W. Castleman, Jr., *J. Chem. Phys.*, 2010, **132**, 044302.
62. E. R. Grumbling and A. Sanov, *J. Chem. Phys.*, 2011, **135**, 164302.
63. D. A. Dahl, *Int. J. Mass Spec.*, 2000, **200**, 3.
64. B. Y. Chang, R. C. Hoetzlein, J. A. Mueller, J. D. Geiser and P. L. Houston, *Rev. Sci. Instrum.*, 1998, **69**, 1665.
65. W. Li, S. D. Chambreau, S. A. Lahankar and A. G. Suits, *Rev. Sci. Instrum.*, 2005, **76**, 063106.
66. M. S. Banna, B. H. McQuaide, R. Malutzki and V. Schmidt, *J. Chem. Phys.*, 1986, **84**, 4739.
67. M. S. Banna, H. Kossmann and V. Schmidt, *Chem. Phys.*, 1987, **114**, 157.

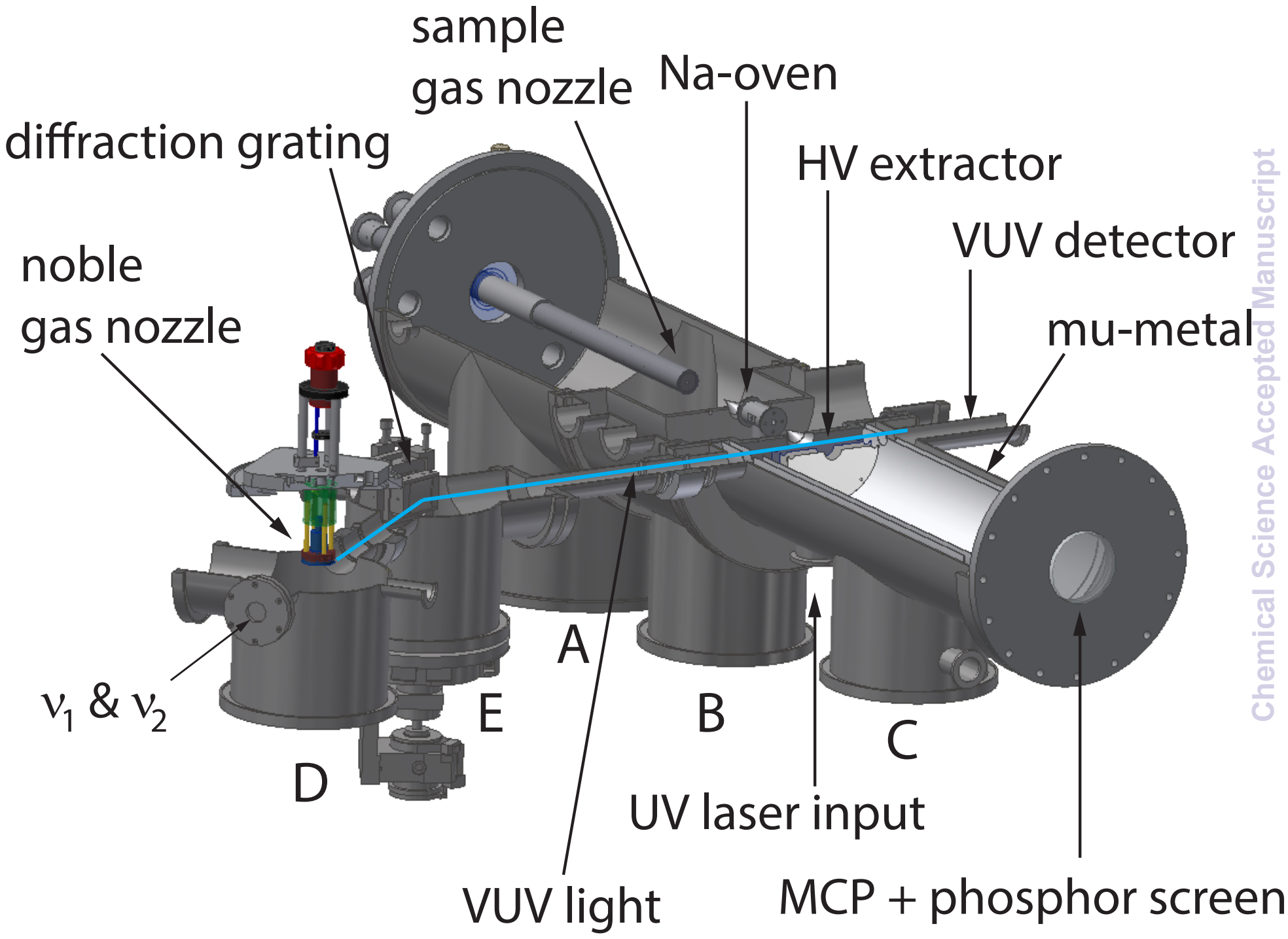

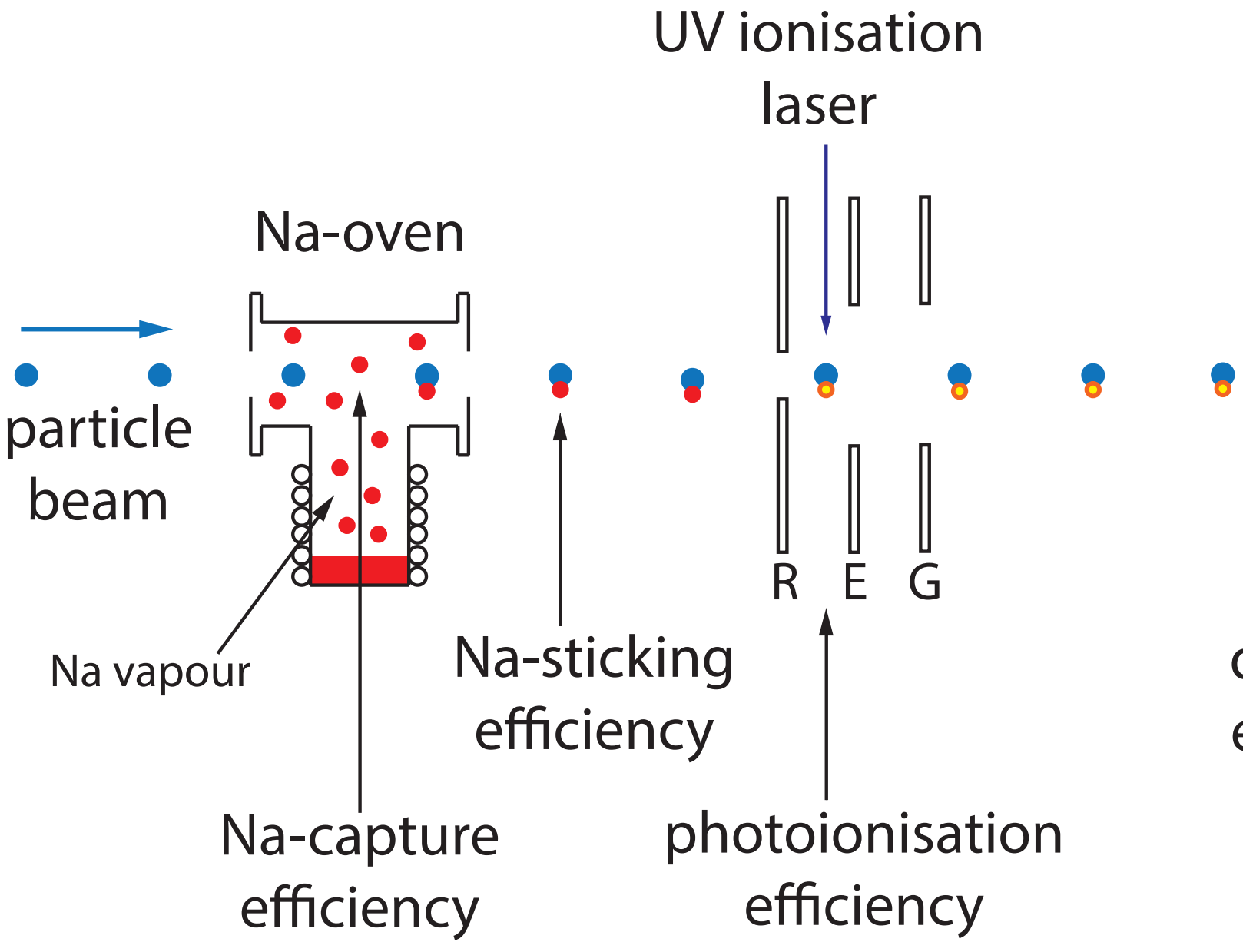

Figure 3

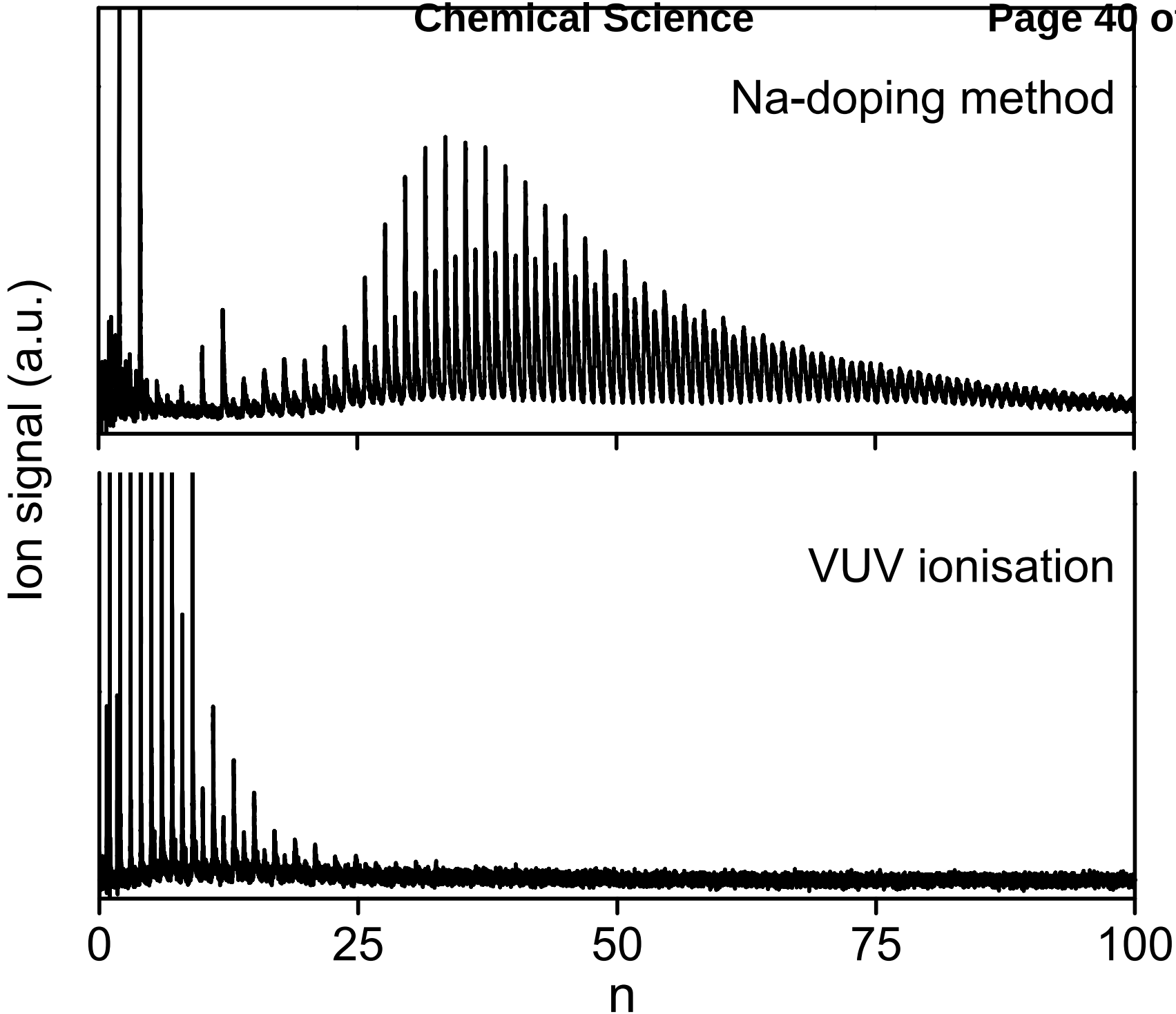

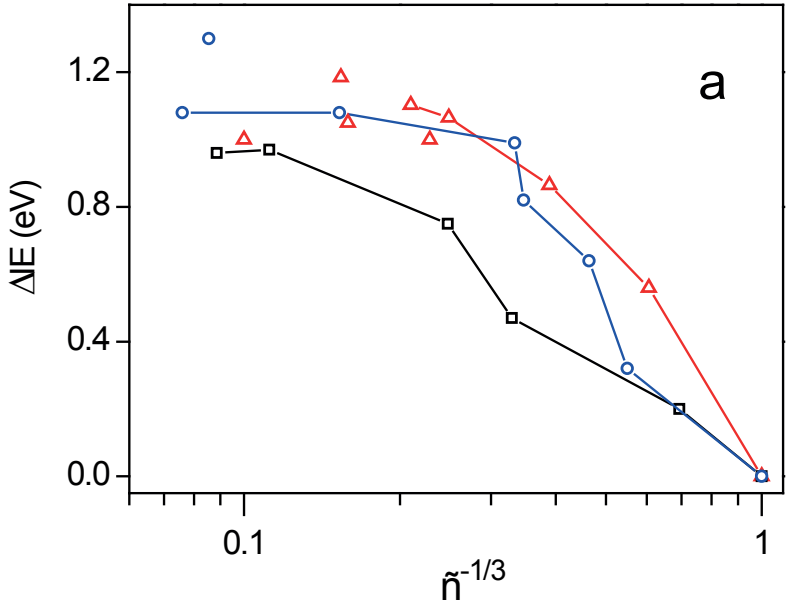

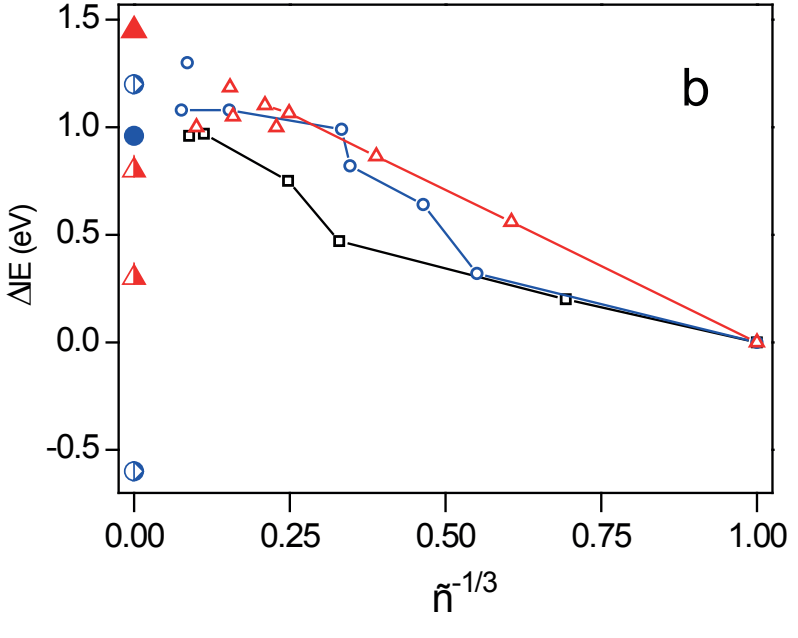

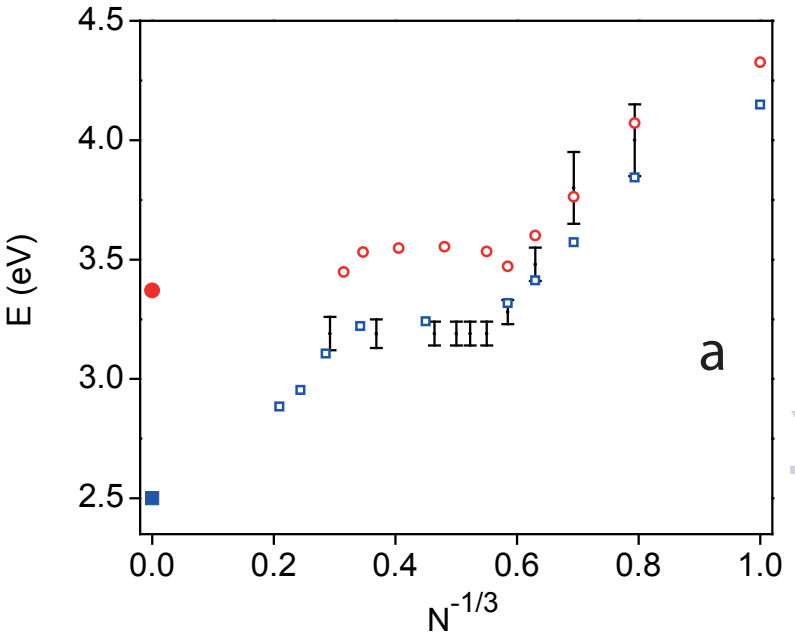

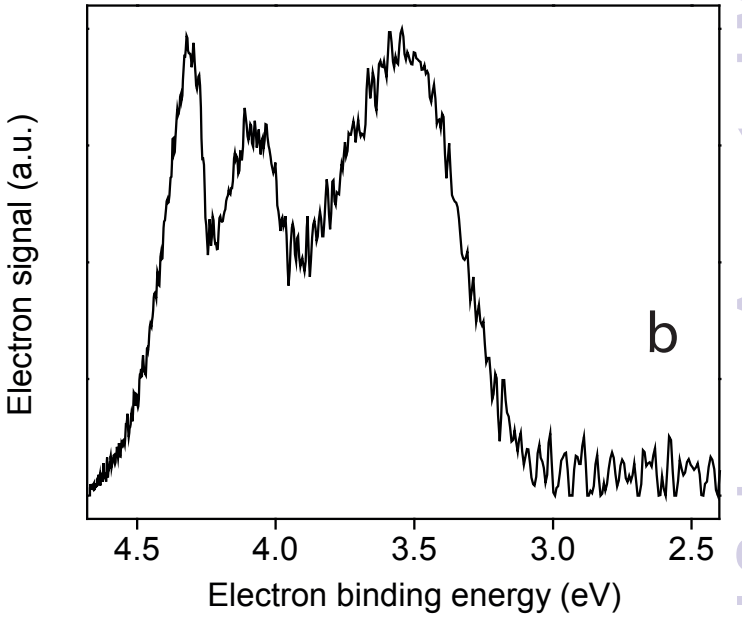

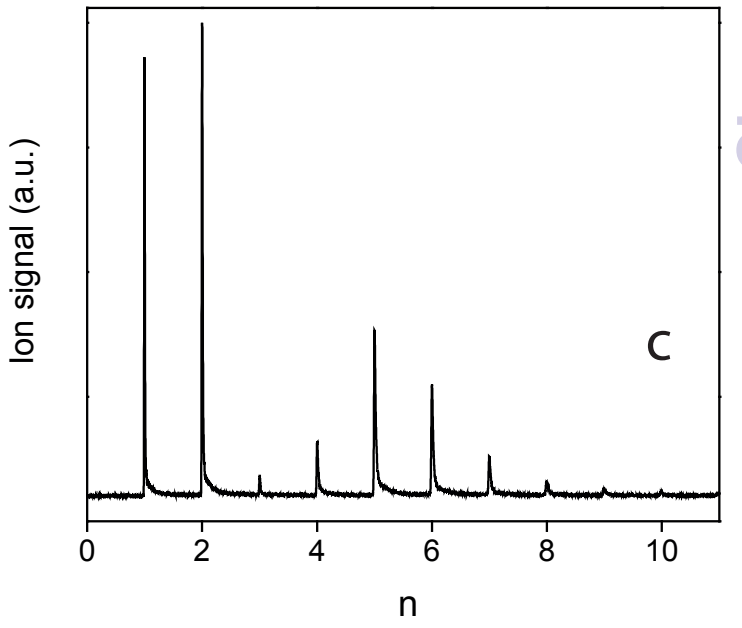

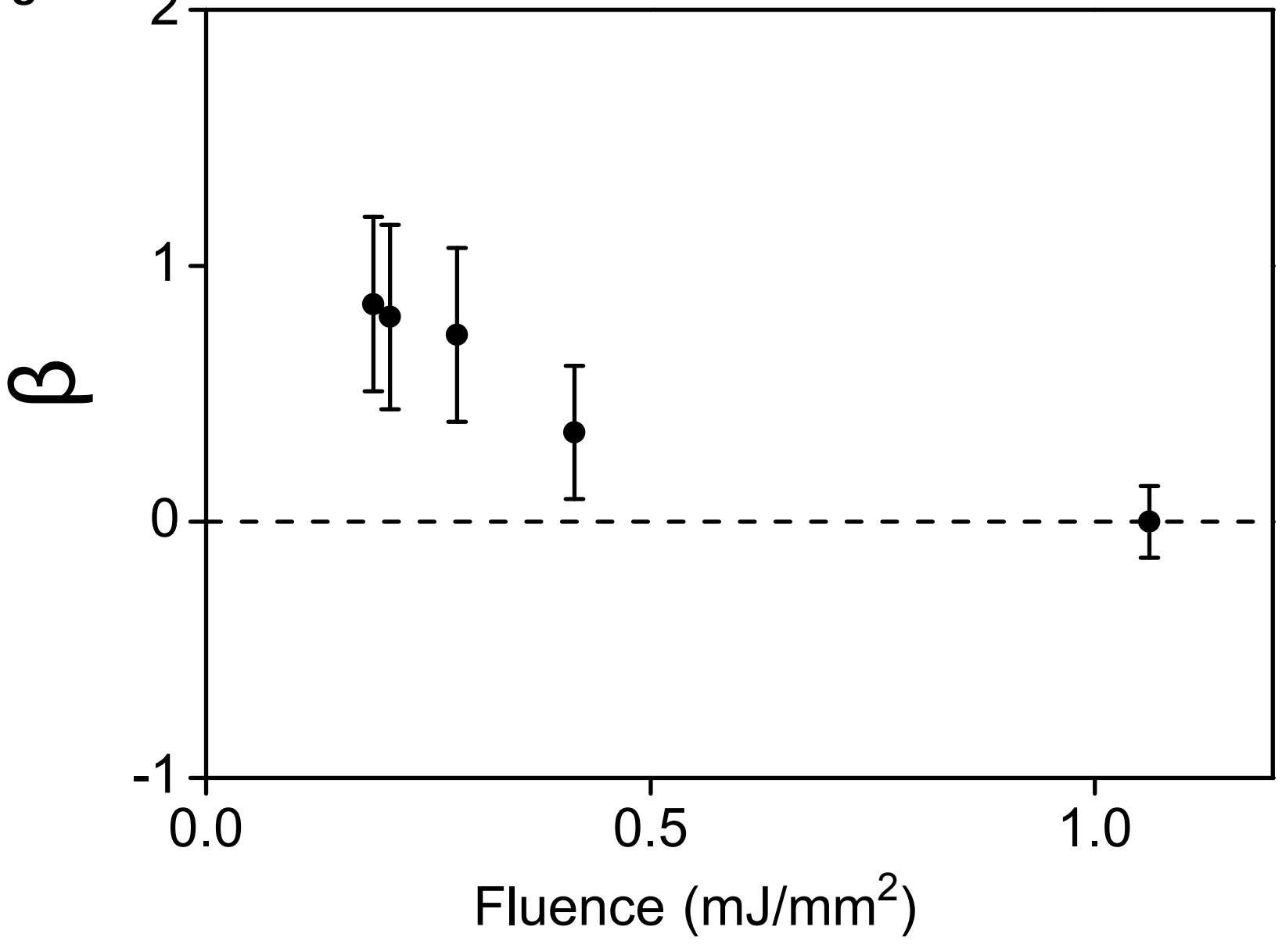

Figure 7

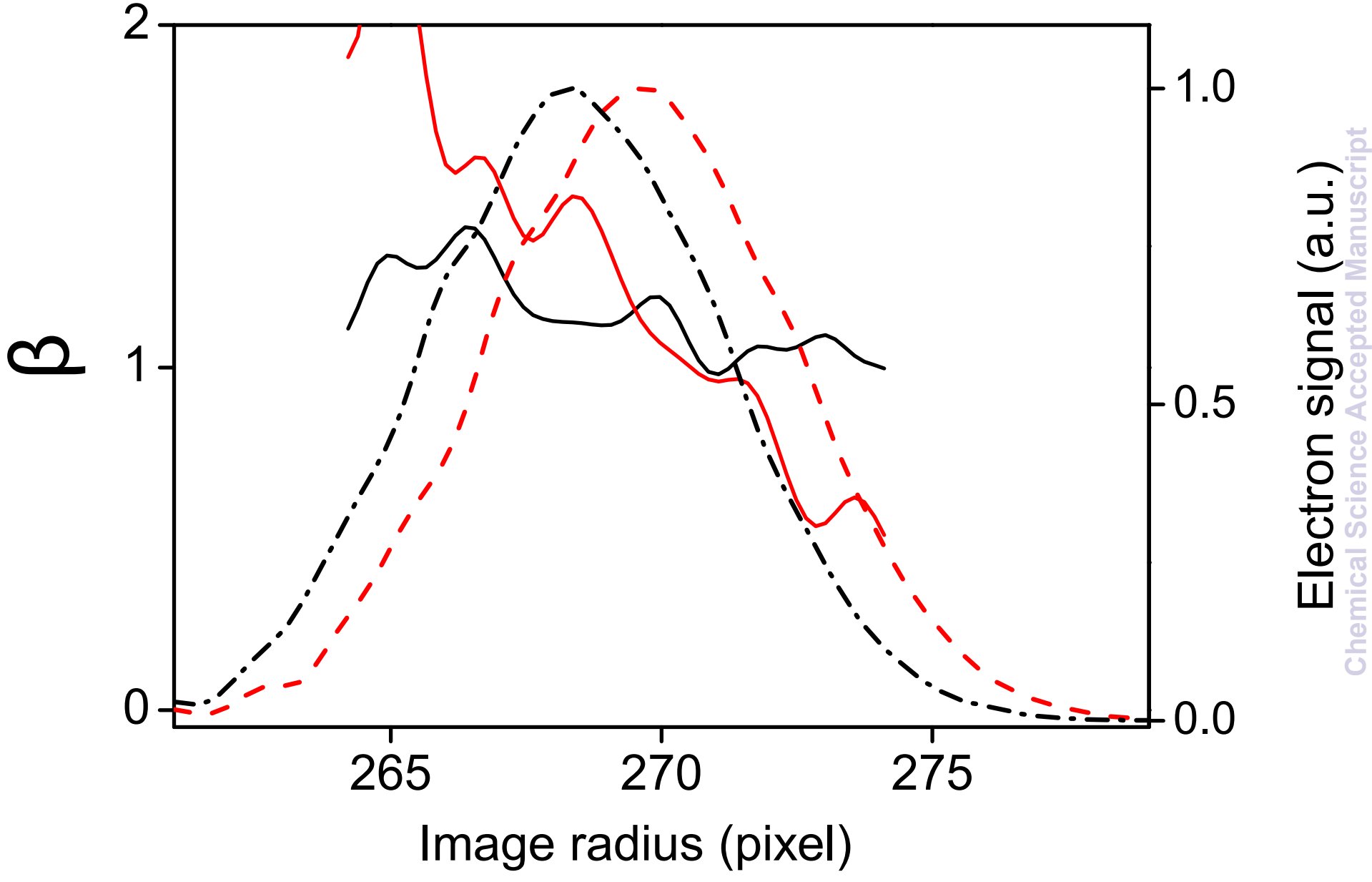

Figure 8